



Dissolution dynamics of a vertically confined sessile droplet

Saptarshi Basu,^{*} D. Chaitanya Kumar Rao , Ankur Chattopadhyay, and Joita Chakraborty 
Department of Mechanical Engineering, Indian Institute of Science, Bangalore 560012, India



(Received 28 July 2020; accepted 16 December 2020; published 5 January 2021)

We experimentally investigate the dissolution of microscale sessile alcohol droplets in water under the influence of impermeable vertical confinement. The introduction of confinement suppresses the mass transport from the droplet to bulk medium in comparison with the nonconfined counterpart. Along with a buoyant plume, flow visualization reveals that the dissolution of a confined droplet is hindered by a mechanism called levitated toroidal vortex. The morphological changes in the flow due to the vortex-induced impediment alters the dissolution rate, resulting in enhancement of droplet lifetime. Further, we have proposed a modification in the key nondimensional parameters [Rayleigh number Ra' (signifying buoyancy) and Sherwood number Sh' (signifying mass flux)] and droplet lifetime τ_e' , based on the hypothesis of linearly stratified droplet surroundings (with revised concentration difference $\Delta C'$), taking into account the geometry of the confinements. We show that experimental results on droplet dissolution under vertical confinement corroborate scaling relations $Sh' \sim Ra'^{1/4}$ and $\tau_e' \sim \Delta C'^{-5/4}$. We also draw attention to the fact that the revised scaling law incorporating the geometry of confinements proposed in the present work can be extended to other known configurations such as droplet dissolution inside a range of channel dimensions, as encountered in a gamut of applications such as microfluidic technology and biomedical engineering.

DOI: [10.1103/PhysRevE.103.013101](https://doi.org/10.1103/PhysRevE.103.013101)

I. INTRODUCTION

The droplet dissolution process involves the dissolution of lighter single or multiple sessile droplets into a bulk medium by means of mass transfer across the liquid-liquid interface. The mass transfer from the low-density droplet is governed by the interplay of convection and diffusion. The contribution of convection becomes dominant when large droplets with low density dissolve into a dense bulk liquid. An understanding of convection-dominated transport process gives more insight into the fundamental mechanisms that are responsible for the characteristic behaviors of multiphase fluid systems. Further control and tailoring of such processes may lead to a variety of modifications that can be implemented in several industrial applications such as chemical waste treatment, separation of heavy metals, food processing, distribution of drugs, and biomedical diagnostics, to name a few [1–5].

From a broader perspective, droplet dissolution can be regarded as a phenomenon analogous to droplet evaporation, which has been extensively investigated by many researchers over the past few decades [6–11]. The sessile droplet evaporation on a solid surface follows one of three different modes depending on surface type and evaporation stage. These modes are constant contact angle (CCA), constant contact radius (CCR), and mixed (combining CCA and CCR) modes of evaporation [12]. The early stage of droplet evaporation usually follows the CCR mode [12,13]. However, it has been shown that both the contact angle and contact radius continuously change in the final stage, where the contact line

velocity abruptly increases for different substrates [13]. The effect of confinement in the evaporation dynamics of sessile droplets has been widely studied and it has been reported that the temporal evolution of the droplets exhibits a universal behavior irrespective of the length of confinement [14,15]. The influence of confinement on evaporating sessile droplets has also been recently investigated for an array of droplets, where it has been shown that the droplet lifetime is a universal function of the degree of confinement for different droplet geometrical parameters (contact angle and contact radius) and surface wettability [16,17]. While the evaporation is considered mostly diffusion driven, the dissolution of a droplet can be governed by either diffusion or buoyancy-driven convection, as reported by Dietrich *et al.* [18]. A transition value of Rayleigh number ($Ra_t \sim 12$) demarcates the two distinguishing regimes. Among different parameters, concentration gradient and size of the droplet (alcohol) have major contributions in controlling the dissolution rate. The complexity of the problem is further amplified, when a multicomponent droplet (water-ethanol) was allowed to dissolve in an oil-rich environment [19]. This article demonstrated dominant solutal Marangoni flow within the droplet. However, in the bulk medium, buoyancy-driven convection was preeminent. Bao *et al.* [20] examined the array of droplets and how the neighboring droplets collectively influence the droplet lifetime. Droplets surrounded by adjacent ones took a longer time to dissolve, while the droplets at the edge have been found to dissolve faster. The computational study by Chong *et al.* [21] demonstrated that the presence of multiple droplets could lead to the large suppression of mass flux. Retardation of dissolution rate has also been reported by other researchers, where they found that increased thickness of the liquid layer

^{*}Corresponding author: sbasu@iisc.ac.in

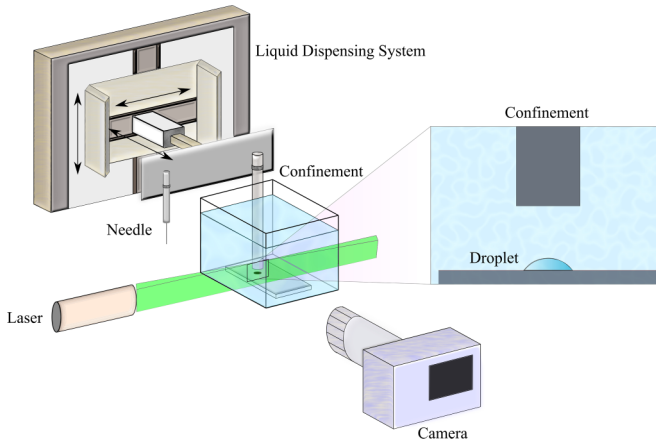


FIG. 1. Schematic of the experimental apparatus for flow visualization.

surrounding the immersed droplet hindered mass diffusion [22,23]. All these articles show that dissolution rates of a single droplet can be manipulated by introducing some sort of spatial confinement, particularly on the same plane the sessile droplet rests. However, none of the systems studied so far have revealed the dissolution dynamics of a vertically confined droplet.

In this work, we report how the overall dissolution dynamics is modified by positioning the confinement on top of a single droplet. Confinement was placed vertically over the droplet in such a manner (refer to Fig. 1) that the movement of the plume, generated due to buoyancy-driven flow, gets obstructed by the impediment. The experiments are carried out on droplets for four different confinement configurations (by varying distance between the droplet and confinement) and their relative contributions in regulating the dissolution rates are assessed both qualitatively as well as quantitatively. We obtain the velocity and vorticity fields surrounding the droplets and discuss the role of a sustained levitated toroidal vortex on the dissolution dynamics of a confined droplet. We provide an estimate of Sherwood number and droplet lifetime as a function of the geometric parameters of the confinement.

II. EXPERIMENTAL METHODOLOGY

In the present work, experiments were conducted with a sessile pentanol droplet, which was allowed to dissolve in a bulk aqueous medium (Fig. 1). The water was kept within a clean acrylic cubic tank ($5\text{ cm} \times 5\text{ cm} \times 5\text{ cm}$) having a volume of 100 mm^3 . A glass slide, coated with a thin PDMS layer, was used as a substrate and was placed at the bottom of the water tank. A single $1.5\text{-}\mu\text{l}$ 1-pentanol droplet (for properties, refer to [18]) was deposited on that substrate with the help of a liquid dispensing system (F200 Flowline, Precore Solutions). Later, the confinement (a cylindrical rod with diameter $\sim 5\text{ mm}$) was positioned over the alcohol droplet within 30 s of droplet deposition. The confinement was designed in such a manner that when it was placed concentric to the droplet, the projected area of the confinement would encompass the entire droplet (Fig. 2). The introduction of the solid confinement creates additional disturbances around the bulk medium near

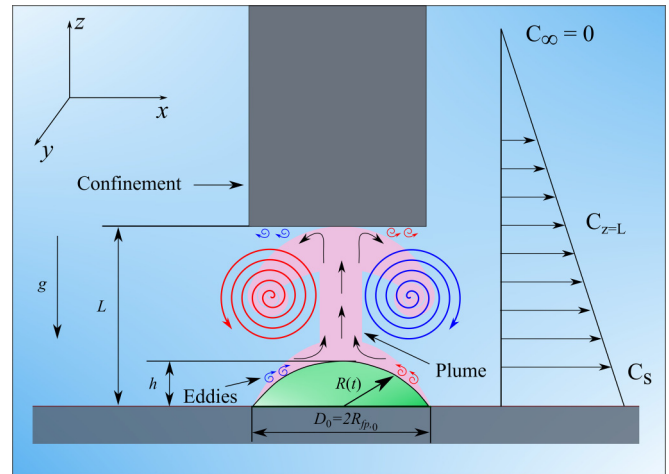


FIG. 2. Schematic representation of the dissolution process of pentanol droplet in water under vertical confinement. The height (L) represents distance between substrate and edge of confinement, and D_0 is initial droplet footprint diameter. Red and blue spiral structures illustrate toroidal vortex while small structures shown on the droplet and at the surface of confinement are eddies.

the drop, however, such unsteady effects decay within $\sim 90\text{ s}$ of its positioning, and bulk medium seems to be stable until the entire dissolution process is over.

The temporal evolution of the dissolving sessile droplet was captured with a charge-coupled device (CCD) camera (Nikon D5600) attached with an adjustable lens (Navitar $8\times$ zoom lens) in presence of a diffused backlight source with a resolution of 6000×4000 pixels having an exposure time of $1/60\text{ s}$. The shadowgraph images were recorded at a rate of one frame per second and postprocessing of shadowgraph images was performed using IMAGEJ software to obtain the evolution of equivalent radius $R(t)$ based on the projected area of the droplet. For visualization of concentration field and flow surrounding the droplet, water in the tank was seeded with neutrally buoyant hollow glass particles ($3\text{--}30\text{ }\mu\text{m}$ diameter). The tracer particles were illuminated using a laser diode beam, which produced a semitelecentric laser line with 15 mm line length, 520 nm wavelength, and 29 mW output power (Schäfter + Kirchhoff GmbH, type 13LT). The linewidth was constant along the laser line and the intensity profile was uniform in line direction. The focal plane of the laser was centered at the sessile droplet. The light reflected by glass particles was visualized by a CCD camera at 24 fps and a spatial resolution of 1920×1080 pixels. The consecutive image pairs were then processed using particle image velocimetry (PIV) software (PIVLAB) with an interrogation window of 64×64 pixels (corresponding to $\sim 40\text{ }\mu\text{m} \times 40\text{ }\mu\text{m}$) to produce time-averaged two-dimensional velocity and vorticity fields. While analyzing the physical flow parameters (volume, radius, etc.) of confined dissolution cases, the initial phase of disturbance has not been included. We have started recording data after about $\sim 120\text{ s}$ ($10\text{--}15\%$ of droplet lifetime) from placing the sessile alcohol drop. Similarly, the velocity and vorticity were obtained for different confined cases after 120 s from the deposition of the droplet for a valid comparison. To keep parity, even in the case of unconfined droplets, the

comparative analysis has been performed from the same time scale. The shadowgraph experiments have been performed at least three times for each confinement and nonconfinement case. The temporal evolution of the droplet radius and volume have been considered by averaging all the trials. Similarly, the flow field data were repeated for a minimum of five runs for corresponding confined and nonconfined cases. The maximum uncertainty in the measurement of droplet radius is $\pm 10 \mu\text{m}$. The maximum uncertainty in velocity and vorticity measurement is $\pm 2\%$.

III. RESULTS AND DISCUSSION

The shadowgraph images of dissolving single pentanol droplet of the same volume ($1.5 \mu\text{l}$) in presence of varying confinement distances ($L/D_0 = 0.75, 1.5, 2.25, 3$) were captured throughout the droplet lifetime and were compared with the nonconfinement case. Figure 2 shows important characteristic features of the dissolution of a droplet under vertical confinement. Here, L is the distance between the substrate and confinement, D_0 is the initial droplet footprint diameter, and $R(t)$ is the equivalent droplet radius at time t . $R(t)$ will be represented as R in the rest of the paper.

The droplet exhibits stick-jump characteristics during dissolution [24,25]. During this stick jump, the footprint diameter remains constant at certain time intervals, which affects the dissolution behavior of the droplet. Therefore, the variation of footprint diameter with time is not considered in the present work. The contact angle hysteresis noted during this sliding event approximately falls between 5° and 10° , considering all the confined and unconfined cases.

Figure 3(a) represents temporal evolution of the equivalent droplet radius (R) normalized with initial droplet radius (R_0) for alcohol droplets at different L/D_0 values. Since R decreases as the droplet dissolves with time, it serves as a relevant parameter for analyzing the droplet evolution with time. Here, time (t) is normalized with the convective time scale, τ_c' (discussed later in the article). Similarly, Fig. 3(b) represents the time evolution of normalized volume, where volume (V) is related to the equivalent radius (R) by the following relation:

$$V = \frac{4}{3}(\pi R^3). \quad (1)$$

It is evident from the figure that compared to the nonconfined case, droplets under confinement dissolve at a slower rate. However, it is rather difficult to distinguish the dissolution rate among the confinement configurations with smaller L/D_0 , which calls for further investigation. Moreover, during the final stage of dissolution, the volume decreases nonlinearly and therefore it has not been quantified in the present work. However, the final stage is rather short with reduced confinement effects with no significant effect on the calculation of Sherwood number and dissolution timescale (as shown later).

The dissolution of solute (alcohol) droplet into the surroundings (water) results in a relatively low-density alcohol-water mixture compared to the dense bulk medium. This unstable stratified zone aids in the formation of a plume (Fig. 3). Further dissolution of the droplet leads to a long tail

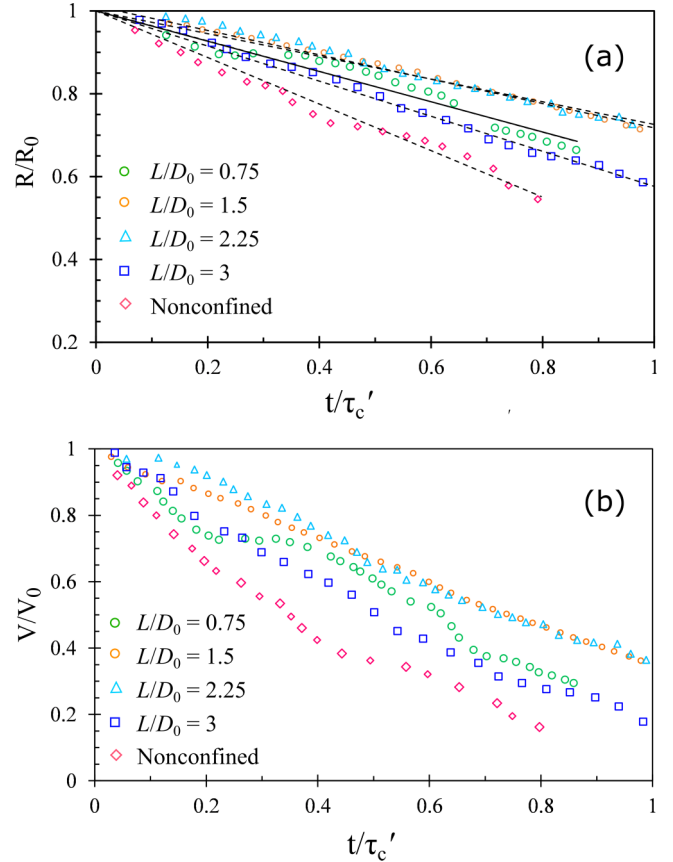


FIG. 3. Comparison of temporal evolution of nonconfined droplet with four different confinement distances ($L/D_0 = 0.75, 1.5, 2.25, \text{ and } 3$), depicting (a) normalized radius as a function of time and (b) normalized volume as a function of time. The time coordinate is normalized with convective lifetime of the droplet (τ_c'). Here, R_0 and V_0 are initial droplet radius and droplet volume, respectively. The curves represent an average of at least three different cases with a maximum uncertainty of $\pm 10 \mu\text{m}$. The dashed lines in (a) represent a linear trend.

of the plume attached to apex of the droplet until entire droplet is dissolved.

A. Flow field visualization

During the dissolution of droplets under confinement, both the large-scale (low-velocity) and small-scale (high-velocity) structures and flow patterns are noticed. Large-scale structures include a toroidal vortex and central plume originating from the droplet apex, while smallest structures are the eddies near the edge of confinement as well as at the interface of droplet surface (Fig. 4). It is important to note that central plume oscillates with time in a stochastic manner, which in turn possibly leads to the deviations in the dissolution rate, particularly for smaller L/D_0 configurations. The formation of small structures (counter-rotating eddies) near the confinement and at the droplet interface is due to the boundary layer. The cascade of these counter-rotating eddies is spatially aperiodically produced at the droplet interface, and are carried upward by the induction of the vortex. Several eddies can be seen distributed along the surface of the droplet [Fig. 4(b)].

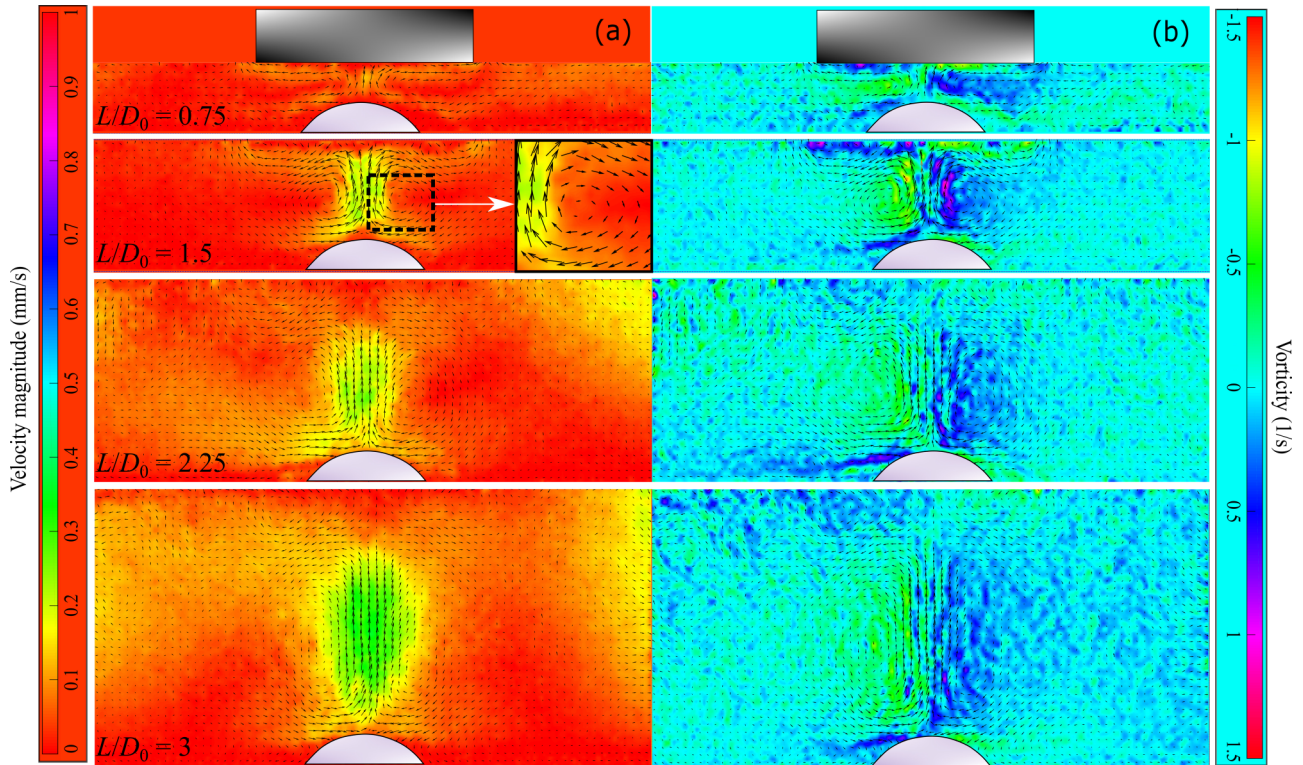


FIG. 4. Flow visualization of dissolving droplets under different confinements ($L/D_0 = 0.75, 1.5, 2.25,$ and 3) representing (a) velocity magnitude and (b) isosurface of vorticity taken at 120 s after the deposition of the droplets. The vectors were obtained by taking a mean over 2 s. The inset in (a) displays the magnified portion of the vortex. The focal plane of the laser was centered at the droplet.

Figures 4(a) and 4(b) visualize the velocity and vorticity fields respectively, corresponding to pentanol droplet dissolution in the presence of four different confinement configurations ($L/D_0 = 0.75, 1.5, 2.25,$ and 3). The interaction of the tip of the plume with the confinement causes it to turn and eventually develop into a vortex entrapping the surrounding bulk medium. Essentially, the plume is divided into streams after it encounters the confinement, which acts as a bluff body to the flow. A portion of its stream dissolves into the surrounding medium while the rest feeds back to the droplet via the vortex [inset of Fig. 4(a), second panel]. As a consequence of this feedback, the local concentration gradient in the droplet surrounding decreases with time, leading to an attenuated mass loss rate from the droplet.

For all the confinement cases, the vortex remains pronounced and stable through most of the droplet lifetime. Figure 5 shows the time-resolved velocity and vorticity fields around pentanol droplets for $L/D_0 = 1.5$. In contrast, for a nonconfined droplet, the vortex convects away leaving behind only the central plume, an observation consistent with Dietrich *et al.* [18].

The diameter of the vortex grows in size (with diameter $\sim 0.65, 1.3, 2.3,$ and 4.2 mm for L/D_0 values of $0.75, 1.5, 2.25,$ and 3 respectively) as the distance between the confinement and droplet is increased. As expected, the time taken for the plume material to complete one rotation and return to its original position is also delayed with L/D_0 (with time $\sim 55, 85, 100,$ and 140 s for L/D_0 values of $0.75, 1.5, 2.25,$ and 3 respectively). This indicates that it takes a shorter amount

of time for the droplet surroundings to be saturated with the alcohol for smaller L/D_0 configurations.

It was observed that the velocity of the plume originating from the apex of the droplet decreases as the confinement is brought closer to the droplet [Fig. 4(a)]. For closer confinement, the plume is shorter with a smaller magnitude of plume velocity $\sim 0.12, 0.2, 0.25,$ and 0.32 mm/s corresponding to L/D_0 values of $0.75, 1.5, 2.25,$ and 3 respectively. For the confinement configuration corresponding to the smallest L/D_0 (0.75), one can observe that the central plume is less noticeable since the velocity magnitude of the flow is significantly lower. If the confinement is very close to the droplet, the plume has less distance available for acceleration. Thus, less momentum is available for transfer and, hence, a weak vortex exists in close confinement [Fig. 4(b), $L/D_0 = 0.75$]. As the confinement height (L) is raised, larger momentum transfer occurs from the accelerating plume to the vortex, making the vortex stronger. As a result, the velocity of the plume increases [Fig. 4(a), $L/D_0 = 1.5$], and a stronger isosurface of vorticity is noticed beside the plume in Fig. 4(b) (second panel, $L/D_0 = 1.5$). At this point, the vortex drags the fluid near the droplet with it, similar to an oversimplified Couette-like flow. Accordingly, counter-rotating eddies occur due to viscosity in the boundary layer of the droplet. A further rise in the confinement height causes the strength of the vortex to reach saturation. This is clear from the isosurface of vorticity in Fig. 4(b) (third panel, $L/D_0 = 2.25$ onwards). This is because, although the plume keeps accelerating, the transferred momentum to the toroidal vortex is further expended in

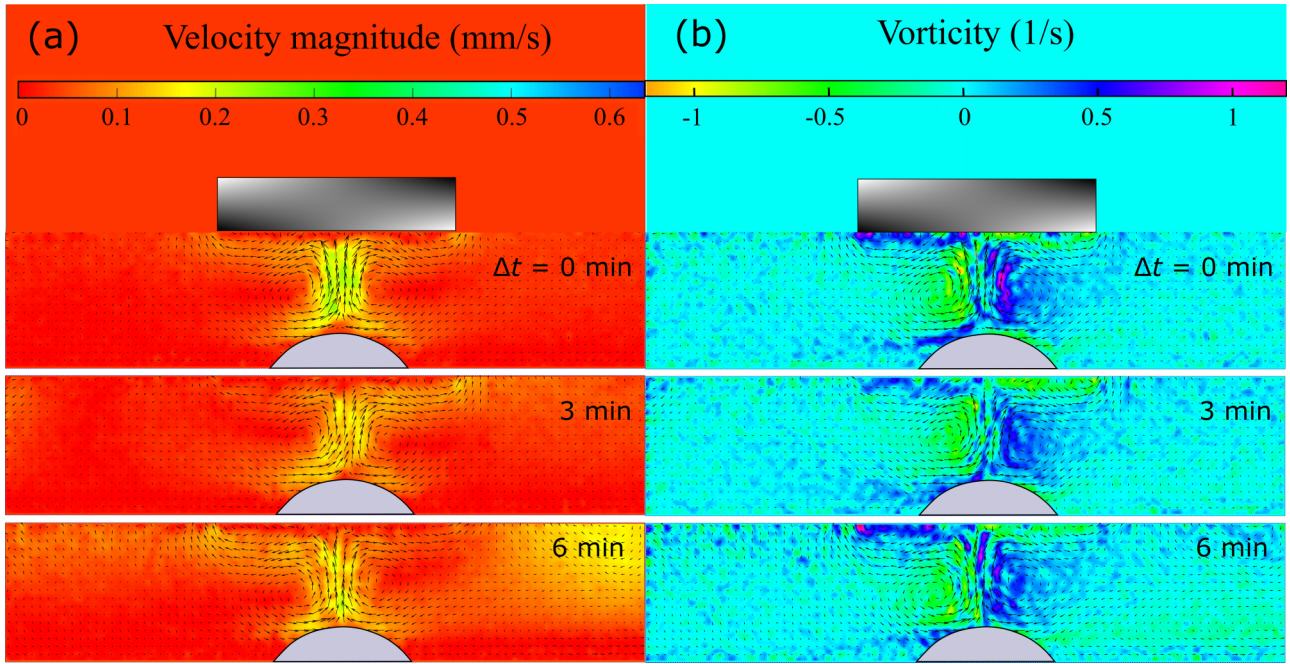


FIG. 5. Flow visualization of a dissolving droplet for confinement $L/D_0 = 1.5$ representing (a) velocity magnitude and (b) isosurface of vorticity taken at $\Delta t = 0, 3,$ and 6 min. The vectors were obtained by taking a mean over 2 s (48 frames).

transporting the eddies from the boundary layer of the droplet upward towards the solid surface of the confinement. As the plume moves upwards, due to momentum diffusion, it drags the surrounding quiescent liquid and leads to gradual growth in velocity boundary layer thickness. Moreover, it was also noticed that the velocity magnitude reduces along with the height of the plume (Fig. 6).

The concentration difference along the plane of the plume can be approximated using linear stratification theory [26]. The bulk medium is considered as an isosolutal semi-infinite fluid reservoir as the mass transfers between the buoyant plume and the droplet surrounding. The plume is lighter and after hitting the confinement, discharges horizontally into the

fluid reservoir (as shown in Figs. 4 and 5). The direction of this discharge remains horizontal (along the plane perpendicular to the plume direction) because the discharge contains more alcohol rich fluid than the rest of the reservoir. The steady-state effect of this discharge is solutal stratification or formation of differential fluid layers having concentration gradients. The dissolution time scale is very large while the discharge rate (\sim mm/sec) is rather quick leading to a quasisteady linearly stratified medium for the majority of the dissolution process.

B. Scaling analysis

Now along with visualization, we can quantify that dissolution rate decreases with decreasing L/D_0 because convective mass transfer decreases. In this fluid system, mass transfer occurs because of concentration difference, hence a relation between total mass flux and (average) concentration difference is required. We express the results using nondimensional numbers such that it can be implemented to system independent applications.

The nondimensional number taking care of this is the Sherwood number (Sh), defined as the ratio of total mass flux to the mass flux by pure diffusion [26]

$$Sh = \frac{\dot{m}_A R}{\mathbf{D} \Delta C}, \tag{2}$$

where \dot{m}_A is the measured mass flux rate ($\text{kg}/\text{m}^2 \text{ s}$) averaged over the droplet surface area (A) of the droplet and \mathbf{D} is the diffusivity coefficient (m^2/s). As discussed before, it is important to note that the buoyant plume fluctuates with time and does not interact with the confinement throughout the droplet lifetime. Therefore, in the present work, the rate of mass loss (\dot{m}_A) from the droplet is evaluated by extracting temporal variation of volume [Fig. 3(b)] averaged over the time considering the

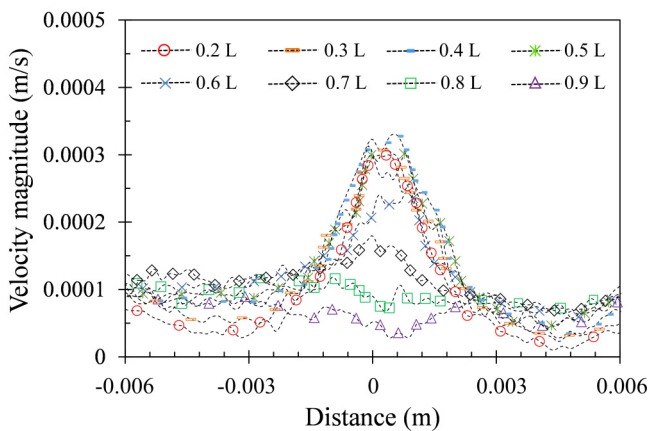


FIG. 6. Velocity magnitude surrounding the dissolving droplet for a confinement configuration ($L/D_0 = 3$) at different heights above the droplet. The distances are measured along the positive z axis.

plume rises from the droplet apex and is in contact with the confinement. The concentration difference ($\Delta C = C_s - C_\infty$) is the difference in the alcohol concentration between the droplet surface location (C_s) and far away from the droplet (C_∞). In Eq. (2), the expression $\frac{D\Delta C}{R}$ accounts for the mass flux due to steady diffusion from a spherical alcohol droplet of radius R ($\theta = 90^\circ$, θ is the equilibrium contact angle). Although in the present study, θ is less than 90° ($25^\circ < \theta < 35^\circ$); the above relation can be used to calculate Sh as no significant differences are observed for the diffusion-limited case in the present range of contact angles [18].

For a nonconfined droplet $C_\infty = 0$, but at the same time, at any finite distance, local concentration will be finite. For any confined case, the concentration at any finite location; say, adjacent to confinement plane ($z = L$) will be nonzero due to linear stratification (Fig. 2) and needs to be estimated precisely.

In order to predict the revised concentration difference ($\Delta C'$), we invoke the linear stratification assumption. The estimation of the local concentrations corresponding to different confinement locations helps us to modify the Sh [given in Eq. (2)] accordingly and the modified Sherwood number (Sh') can be expressed as

$$Sh' = \frac{\dot{m}_A R_0}{D \Delta C'}. \quad (3)$$

The amended concentration difference is represented by $\Delta C' = C_s - C_{z=L}$, thereby taking into account the difference in alcohol concentration between the droplet surface location ($z = 0$) and at the edge of confinement ($z = L$). The alcohol concentration along the plane of confinement is $C_{z=L} = C_s \times (h_0/L)$, where h_0 is the droplet height during the start of the dissolution and L is the distance between the substrate and the confinement (Fig. 2). The expression for $C_{z=L}$ is consistent with respect to the limits on L . When the length of the confinement is very large, ($L \gg h_0$, $L \rightarrow \infty$), the local concentration approaches the unconfined case, i.e., $C_{z=L} = C_\infty = 0$ and when the length of the confinement approaches droplet height ($L \rightarrow h_0$), the local concentration approaches the alcohol concentration at the surface of the droplet, i.e., $C_{z=L} = C_s$.

Similar to the Sherwood number (Sh'), the revised Rayleigh number (the ratio of the buoyant force to the damping force) can be expressed as [26]

$$Ra' = \frac{g\beta\Delta C'R_0^3}{\nu D}, \quad (4)$$

where g is the acceleration due to gravity (m/s^2), β indicates the solutal expansion coefficient (m^3/kg) and ν represents the kinematic viscosity (m^2/s). To incorporate the effect of geometric dependence (confinement), we have modified the concentration difference by invoking the linear stratification assumption (discussed earlier),

$$Ra' = Ra \times f(D/L), \quad (5)$$

where the scaling function $f(D/L)$ can be represented as

$$f(D/L) = 1 - \frac{h_0}{L} \quad \text{and} \quad h_0 = \alpha D_0 \tan(\theta/2). \quad (6)$$

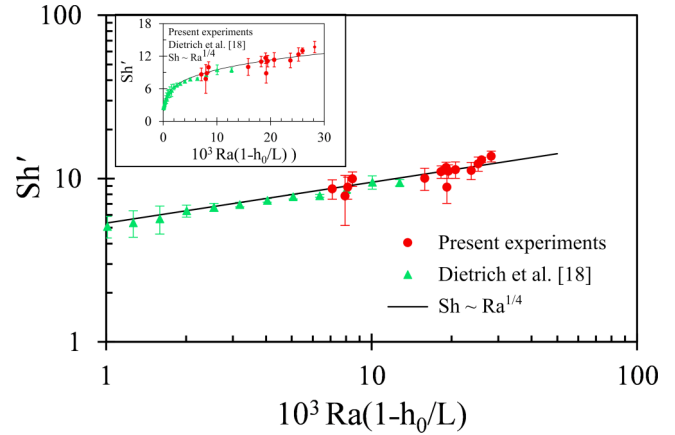


FIG. 7. Sherwood number (Sh') as a function of Rayleigh number (Ra') for the present experiments along with the results of Dietrich *et al.* [18]. The plot shows the average value and the solid line represents $Sh = Ra^{1/4}$. The modified Rayleigh number, Ra' is expressed as a function of geometrical parameters taking linear stratification into consideration, where h_0 is the initial droplet height and L is the confinement distance. Inset shows a variation of Sh' against Ra' considering the lower range of Ra' in Dietrich *et al.* [18] and higher range of Ra' in the present work.

In Eq. (6), D_0 indicates the footprint diameter of the droplet at the inception of dissolution and θ is the equilibrium contact angle of pentanol on Polydimethylsiloxane (PDMS) substrate ($\theta \sim 30^\circ$). Here, α is a constant and it is equal to 0.95 [27]. Figure 7 shows the Sh' as a function of Ra' for all cases (nonconfinement and confined ones), indicating that the data follow $Sh' \sim Ra'^{1/4}$ scaling. This observation is consistent with the results reported by Dietrich *et al.* [18] for nonconfined droplets where the Rayleigh number (Ra) and Sherwood number (Sh) are obtained by changing the size and material property of deposited droplet. However, in the present work, the primary focus is to study the influence of confinement on the dissolution process. Hence Ra' and Sh' are computed by introducing vertical confinement and changing its distance from the droplet while keeping all other parameters constant. It was observed that Sh' increases with Ra' signifying a rise in convection dominated mass transfer (thus faster rate of dissolution). The results imply that, by introducing confinement close to the droplet, the local alcohol concentration increases, thereby leading to a steady decline in the total mass transfer rate. The figure confirms the comprehensive applicability of the scaling function in the context of droplet dissolution under confinement as well as nonconfinement. The solid line represented in Fig. 7 denotes the relation $Sh \sim Ra^{1/4}$ for convection dominant dissolution [26].

As it is established from the ongoing discussion that the dominant mechanism of mass transfer in the present case is via convection, it is important to calculate the time (τ_c') taken by the droplet to completely dissolve into the bulk. Although during dissolution, the radius decreases with time, this can be neglected by assuming the process to be quasistatic. The rate of mass loss $\dot{m}_A \sim -R^2 \rho \left(\frac{dR}{dt}\right)$ from the pentanol droplet is expected to be of the same order as that of the mass $\dot{m}_p = \frac{AD\Delta C' Sh'}{R}$ carried away by the plume over the entire area (A) of

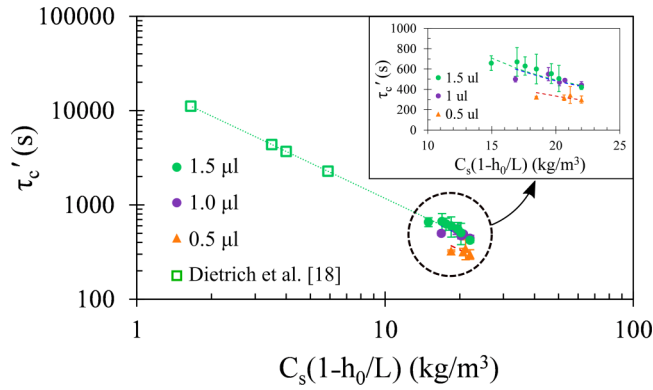


FIG. 8. The variation of dissolution time is plotted as a function of the concentration difference for pentanol droplets of different volume (1.5, 1, and 0.5 μl). The data presented in open symbol correspond to different liquids (1-hexanol, 1-heptanol, 2-heptanol, and 3-heptanol), estimated using the concentration values taken from Dietrich *et al.* [18]. The dotted lines represent the theoretical dissolution time obtained from Eq. (8) for the respective droplet volumes. The modified concentration difference $\Delta C'$ is expressed as a function of geometrical parameters considering linear stratification. Additionally, inset is provided for proper distinction of present experimental data.

the droplet-bulk interface [18]. We will obtain the following relation by equating both of them:

$$\frac{dR}{dt} = -a \left(\frac{g\beta\Delta C'^5 \mathbf{D}^3}{\nu\rho^4 R} \right)^{1/4}, \quad (7)$$

after integration of R from $R = R_0$ to $R = 0$, and time from $t = 0$ to $t = 0$ to $t = \tau_c'$ gives the dissolution time,

$$\tau_c' = \frac{4}{5a} \left(\frac{\nu\rho^5 R_0^5}{g\beta\Delta C'^5 \mathbf{D}^3} \right)^{1/4}, \quad (8)$$

where R_0 is the droplet radius at the beginning of the dissolution process and ρ is the density of pentanol. It turns out from Eq. (8) that for a given volume of droplet undergoing dissolution in a bulk, the droplet lifetime has inverse dependence on the concentration gradient, i.e., $\tau_c' \propto \Delta C'^{-5/4}$. Here, the material-dependent prefactor “ a ” assumes a constant value of 10.5 for all the cases. The measured (experimental) values of the droplet lifetime for the confined cases (with

additional values of $\Delta C'$ corresponding to 1.5-, 1-, and 0.5- μl droplets) and the nonconfinement cases are compared against the theoretical relation [calculated by Eq. (8)], showing a good degree of agreement (Fig. 8).

It is important to note that, in the present work, a linearly stratified medium is considered assuming the volume of the container and thus the medium is much larger than the droplet volume during the dissolution process. In addition, the width of the confinement is equal to or larger than the confinement. For the cases where the width of the confinement is smaller than the droplet, there is a possibility that the plume would not effectively interact with the confinement and eventually affect the feedback to the droplet. Moreover, the linear stratification theory can only be applied to the droplets which result in the emission of the plume and hence undergo convection-dominated dissolution. For example, when $Ra < 12.1$ and $Sh < 1.2$, the dissolution process is diffusion dominated [18], therefore, the plume does not exist to create a linearly stratified medium.

IV. CONCLUSION

To summarize, in this work we have shown that placing vertical confinement over a dissolving droplet is one of the probable means to control its mass flux. The introduction of confinement suppresses mass flux compared to the nonconfined case and delays the time required for the droplet to completely dissolve. In fact, nearer the confinement (smaller L/D_0), more is the time taken by the alcohol droplet to dissolve. We report the coupling of the plume and toroidal vortex, where a part of the plume dissolves into the surrounding medium, while the rest feeds back to the droplet via the vortex. Due to this feedback, local concentration difference surrounding the droplet decreases with time. We have formulated a method by invoking the linear stratification assumption to estimate local concentration difference and subsequently propose modified nondimensional numbers. We estimate Sh' , Ra' , and τ_c' for different geometrical configurations (L/D_0) and both the confined as well as nonconfined droplets have been found to follow the scaling relations, $Sh' \sim Ra'^{1/4}$ and $\tau_c' \sim \Delta C'^{-5/4}$. The present work also signifies that, by using the scaling function $(1 - \frac{h_0}{L})$, we can uniquely evaluate mass transfer properties pertaining to similar vertical confinements (with confinement width larger than droplet footprint diameter) and liquid properties.

- [1] K. Fukumoto, M. Yoshizawa, and H. Ohno, *J. Am. Chem. Soc.* **127**, 2398 (2005).
- [2] P. Chasanis, M. Brass, and E. Y. Kenig, *Int. J. Heat Mass Transfer* **53**, 3758 (2010).
- [3] Z. Lu, A. Rezk, F. Jativa, L. Yeo, and X. Zhang, *Nanoscale* **9**, 13441 (2017).
- [4] A. Jain and K. K. Verma, *Anal. Chim. Acta* **706**, 37 (2011).
- [5] D. Lohse and X. Zhang, *Rev. Mod. Phys.* **87**, 981 (2015).
- [6] R. G. Picknett and R. Bexon, *J. Colloid Interface Sci.* **61**, 336 (1977).
- [7] R. D. Deegan, O. Bakajin, T. F. Dupont, G. Huber, S. R. Nagel, and T. A. Witten, *Nature (London)* **389**, 827 (1997).
- [8] N. Shahidzadeh-Bonn, S. Rafai, A. Azouni, and D. Bonn, *J. Fluid Mech.* **549**, 307 (2006).
- [9] A. M. J. Edwards, P. S. Atkinson, C. S. Cheung, H. Liang, D. J. Fairhurst, and F. F. Ouali, *Phys. Rev. Lett.* **121**, 184501 (2018).
- [10] H. Kim, K. Muller, O. Shardt, S. Afkhami, and H. A. Stone, *Nat. Phys.* **13**, 1105 (2017).
- [11] Y. Li, C. Diddens, P. Lv, H. Wijshoff, M. Versluis, and D. Lohse, *Phys. Rev. Lett.* **122**, 114501 (2019).
- [12] A. M. Cazabat and G. Guena, *Soft Matter* **6**, 2591 (2010).

- [13] E. Y. Gatapova, A. M. Shonina, A. I. Safonov, V. S. Sulyaeva, and O. A. Kabov, *Soft Matter* **14**, 1811, (2018).
- [14] L. Bansal, S. Hatte, S. Basu, and S. Chakraborty, *Appl. Phys. Lett.* **111**, 101601 (2017).
- [15] L. Bansal, S. Chakraborty, and S. Basu, *Soft Matter* **13**, 969 (2017).
- [16] S. Hatte, K. Pandey, K. Pandey, S. Chakraborty, and S. Basu, *J. Fluid Mech.* **866**, 61 (2019).
- [17] K. Pandey, S. Hatte, K. Pandey, S. Chakraborty, and S. Basu, *Phys. Rev. E* **101**, 043101 (2020).
- [18] E. Dietrich, S. Wildeman, C. W. Visser, K. Hofhuis, E. Stefan Kooij, H. JW Zandvliet, and D. Lohse, *J. Fluid Mech.* **794**, 45 (2016).
- [19] H. Tan, C. Diddens, A. A. Mohammed, J. Li, M. Versluis, X. Zhang, and D. Lohse, *J. Fluid Mech.* **870**, 217 (2019).
- [20] L. Bao, V. Spandan, Y. Yang, B. Dyett, R. Verzicco, D. Lohse, and X. Zhang, *Lab Chip* **18**, 1066 (2018).
- [21] K. L. Chong, Y. Li, C. Shen Ng, R. Verzicco, and D. Lohse, *J. Fluid Mech.* **892**, A21 (2020).
- [22] Q. Xie and J. Harting, *Soft Matter* **15**, 6461 (2019).
- [23] X. Li, Y. Wang, B. Zeng, Y. Li, H. Tan, H. J. W. Zandvliet, X. Zhang, and D. Lohse, *Langmuir* **34**, 10659 (2018).
- [24] E. Dietrich, E. Stefan Kooij, X. Zhang, H. JW Zandvliet, and D. Lohse, *Langmuir* **31**, 4696 (2015).
- [25] X. Zhang, J. Wang, L. Bao, E. Dietrich, R. CA van der Veen, S. Peng, J. Friend, H. JW Zandvliet, L. Yeo, and D. Lohse, *Soft Matter* **11**, 1889 (2015).
- [26] A. Bejan, *Convection Heat Transfer* (Wiley, New York, 2013).
- [27] M. R. Alsan and H. Y. Erbil, *Langmuir* **14**, 1915 (1998).